Role of time reversal symmetry and tilting in circular photogalvanic responses

Banasree Sadhukhan[1,2,*] and Tanay Nag[3,†]

[1]*KTH Royal Institute of Technology, AlbaNova University Center, SE-10691 Stockholm, Sweden*

[2]*Leibniz Institute for Solid State and Materials Research IFW Dresden, Helmholtzstrasse 20, 01069 Dresden, Germany*

[3]*SISSA, via Bonomea 265, 34136 Trieste, Italy*

(Received 23 November 2020; accepted 19 April 2021; published 28 April 2021)

We study the role of time reversal symmetry (TRS) in the circular photogalvanic (CPG) responses considering a chiral Weyl semimetal (WSM), while a quantized CPG response is guaranteed by both the broken inversion symmetry and broken mirror symmetries. The TRS broken WSM yields one left and one right chiral Weyl node (WN), while there are two left and right chiral WNs for a TRS invariant WSM. We show that these features can potentially cause the quantization of a CPG response at higher values compared to the topological charge of the underlying WSM. This is further supported by the fact that Berry curvature and velocity behave differently depending on whether the system preserves or breaks the TRS. We find the CPG responses for a TRS invariant type-II WSM to be quantized at two and four times the topological charge of the activated WNs while the chemical potentials are, respectively, chosen in the vicinity of the energies associated with the left and right chiral WNs. By contrast, irrespective of the above choice of the chemical potential, the quantization in the CPG response is directly given by the topological charge of the activated WNs for the TRS broken case. Interestingly, we notice a nonquantized peak in the CPG response when the energies of the WNs associated with opposite chiralities are close to each other, as is the case for the TRS invariant type-I WSM considered here. Moreover, we show that the tilt can significantly modify the CPG response as the velocity in the tilt direction changes, which enters into the CPG tensor through the Fermi distribution function. Given these exciting outcomes, the second-order CPG response emerges as a useful indicator to characterize the system under consideration. Furthermore, we investigate the momentum resolved structure of the CPG response to relate with the final results and strengthen our analysis from the perspective of the lattice models.

DOI: 10.1103/PhysRevB.103.144308

I. INTRODUCTION

The Weyl semimetals (WSMs) [1–3] have drawn huge attention in recent years due to their exotic properties that are mainly caused by the unusual Fermi arc surface states and chiral anomaly [4]. It has been found in WSMs that nontrivial band crossing occurs at an even number of discrete points in the Brillouin zone. These special gap closing points, protected by some crystalline symmetry, are referred as Weyl nodes (WNs) and they carry a topological charge (referred as Chern number), which is a quantized Berry flux through the Fermi surface enclosing it in momentum space [4]. It is important to mention here that upon breaking of either time reversal symmetry (TRS) or inversion symmetry (IS), or both of these symmetries, in Dirac semimetals, each twofold degenerate Dirac cone reduces to two isolated WNs of opposite chiralities [5]. In particular, there exist a minimum of two WNs of opposite chirality when the system breaks the TRS; four WNs are noticed, in general, for a system with only broken IS [6]. The conical spectrum and the pointlike Fermi surface at the WN are the signature of an untilted WSM, namely, type-I WSMs. An interesting situation arises when large tilting of the Weyl cone results in a Lifshitz transition. This leads to a new class of materials called type-II WSMs, where the Fermi surface is no longer pointlike [7]. These WSM phases have been realized experimentally in several inversion asymmetric compounds (TaAs, $MoTe_2$, WTe_2) [8–12].

As expected, topological systems become fertile ground for investigating various quantum topological electromagnetic responses [13–17]. The chiral-anomaly related negative magnetoresistance and the quantum anomalous Hall effect are the immediate upshot of the topological nature of WSMs [15,18,19]. Apart from the electric transport, the exotic signatures associated with WSMs show up in the thermal responses, which have been studied theoretically [20–23] and experimentally [24,25]. On the other hand, thanks to the distinct behavior of the density of states at the Fermi level, it has been shown that the electronic and thermal transport properties of type-II WSMs become markedly different from that associated with type-I WSMs [26–30]. In addition to the linear optical responses, the higher order optical responses, such as the circular photogalvanic effect (CPGE) [31–39] and difference frequency generation [40], are found to be very interesting for chiral topological crystals, where the mirror symmetry is broken in addition to inversion symmetry, resulting in nondegenerate WNs. Topological chiral semimetals (SMs) can be realized in many multifold fermions such as the transition metal monosilicides MSi (M = Co, Mn, Fe, Rh) [41–43],

*banasree@kth.se

†tnag@sissa.it

double WSMs $HgCr_2Se_4$ and $SrSi_2$ [44–47], and triple WSMs such as $A(MoX)_3$ (with $A = Rb,TI$; $X = Te$) [48].

It is important to have nondegenerate WNs to obtain interesting chiral transport behavior [31,49]. Very interestingly, the quantized behavior of the CPG response, which is a DC photocurrent switching with the sense of circular polarization of the incident light, happens to be a direct experimental probe to measure the Chern numbers in topological semimetals [50]. Very recently, a giant nonquantized photogalvanic effect has been reported in the noncentrosymmetric type-II Weyl semimetal TaAs family [33,34], where degenerate WNs exist in the presence of mirror symmetry. The dipole moment of Berry curvature also leads to the nonlinear Hall effect, where nonquantized responses are observed [51]. Moreover, the interaction also leads to a nonquantized nonlinear response [52].

Given the background of the higher order responses, here we probe the effect of TRS on the second-order chiral transport, namely, the CPG response considering IS broken type-I and type-II WSMs. The CPG response is found to exhibit a quantized response proportional to the topological charge of the WNs when the underlying untilted WSM breaks TRS, IS, and mirror symmetries. The Pauli blocking mechanism controls the behavior of the CPG response where only one WN would participate in the transport and the other WN with opposite chirality remains inactive. Our aim is to investigate the CPG response when the underlying WSM, preserving the TRS, possesses four WNs. The questions that we would like to precisely answer are the following: Is the CPG response always proportional to the topological charge of the underlying WSM? Does the number of WNs matter? How can the CPGE distinguish between type-I and type-II WSMs with and without TRS? Although much exploration has been done regarding the nonquantized behavior of the CPGE in the presence of degenerate WNs, here we present our analysis of the nature of the quantized response in the CPGE in the presence of TRS.

In this work, we consider TRS broken and invariant type-I and type-II WSMs to investigate the CPG response. We find that in general, the tilt can modify the CPG response as compared to the untilted case. The TRS broken WSM with two WNs shows a quantized CPG response, irrespective of the tilt, except a few dissimilarities. The magnitude of the quantization here is proportional to the topological charge of a single WN. Interestingly, for a TRS invariant type-II WSM with four WNs, the CPG response can only become quantized, while for a type-I WSM, it becomes nonquantized. The magnitude of quantization depends on both the number of WNs and the topological charge associated with each WN. We find that the CPGE exhibits a nonquantized peak instead of a quantized plateau when the energy gap between the WNs with opposite chiralities is vanishingly small, as is the case for a TRS invariant type-I WSM. Unlike the TRS broken case where the CPG trace becomes quantized to two opposite values of the same magnitude once the chemical potential is chosen close to the energies of two opposite chiral WNs, the CPG trace exhibits quantization to two different values (two and four times the topological charge) with opposite signs for a TRS invariant WSM. These can be caused by the structure of the Berry curvature and velocity for TRS invariant WSMs that become different as compared to the TRS broken WSMs. Moreover, the window of quantization changes substantially depending on the activated WNs in the case of TRS invariant WSMs. We also study the momentum resolved CPG trace to further appreciate the numerical results obtained from the lattice models.

The paper is organized as follows. In Sec. II, we describe the CPG response and introduce the TRS invariant, TRS broken lattice model. Next, in Sec. III, we discuss our numerical results obtained from the lattice model and understand them from the perspective of the low-energy model. Finally, in Sec. IV, we conclude with possible future direction.

II. FORMALISM AND MODEL

A. Circular photogalvanic effect (CPGE)

The CPG injection current is a second-order optical response when the system is irradiated with the circularly polarized light. It is defined as

$$\frac{dJ_i}{dt} = \beta_{ij}(\omega)[\mathbf{E}(\omega) \times \mathbf{E}^*(\omega)]_j, \tag{1}$$

where $\mathbf{E}(\omega) = \mathbf{E}^*(-\omega)$ is the circularly polarized electric field of frequency ω, and the i and j indices are the direction of the current J_i and circular polarized light field, respectively. This optical activity is originated from the interband electronic transition. The tensor β_{ij} is purely imaginary and only nonzero if the IS is broken. In chiral topological semimetals where inversion and all mirror symmetries are broken, WNs appear at different energies. In this case, the trace of β_{ij} is quantized for a finite range of frequencies. On the other hand, if the system possesses at least one mirror symmetry, then all the diagonal components of β_{ij} vanish, leaving the nonquantized CPG response from the off-diagonal component of β_{ij} [33]. The CPG tensor β can be written in general as [31,53]

$$\beta_{ij}(\omega) = \frac{\pi e^3}{\hbar V}\epsilon_{jkl}\sum_{\boldsymbol{k},n,m}\Delta f_{\boldsymbol{k},nm}\Delta v^i_{\boldsymbol{k},nm}r^k_{\boldsymbol{k},nm}r^l_{\boldsymbol{k},mn} \times \delta(\hbar\omega - E_{\boldsymbol{k},mn}), \tag{2}$$

where V is the sample volume, $E_{\boldsymbol{k},nm} = E_{\boldsymbol{k},n} - E_{\boldsymbol{k},m}$ and $\Delta f_{\boldsymbol{k},nm} = f_{\boldsymbol{k},n} - f_{\boldsymbol{k},m}$ are the difference between nth and mth band energies and Fermi-Dirac distributions respectively, $\mathbf{r}_{\boldsymbol{k},nm} = i\langle n|\partial_{\boldsymbol{k}}|m\rangle$ is the off-diagonal Berry connection, and $\Delta v^i_{\boldsymbol{k},nm} = \partial_{k_i}E_{\boldsymbol{k},nm}/\hbar = v_{i,n} - v_{i,m}$.

It is pertinent to discuss the relation between the response coefficient and the incident applied intensity. Let us consider the electric fields in the x-y plane, $\mathbf{E} = |E|(1, i, 0)/\sqrt{2}$. Therefore, the injection current induced in the z direction is given by

$$\partial_t J_z = \beta_{zz}[\mathbf{E}(\omega) \times \mathbf{E}^*(\omega)]_z = i\beta_{zz}|E|^2 n_z, \tag{3}$$

with $n_z = (0, 0, 1)$. The total injection current can be obtained by adding up the contributions from the three orthogonal directions: $\partial_t J_T = (\beta_{xx} + \beta_{yy} + \beta_{zz})i|E|^2$. Under the reversal of polarization of the incident light i.e., $i \to -i$, the injection current changes its sign. Therefore, by experimentally measuring the injection current, one can directly estimate the CPG response that is encoded in the CPG tensor $\mathrm{Tr}[\beta(\omega)]$.

The above CPG tensor reduces to a very tractable form for a two-band model where $n, m = 1, 2$. Following an analytical computation of the CPG coefficient, one can find the trace CPG tensor β_{ij} for a two-band model,

$$\mathrm{Tr}[\beta(\omega)] = \frac{i\pi e^3}{\hbar^2 V}\sum_{\boldsymbol{k}} \Delta f_{\boldsymbol{k},12}\partial_{k_i} E_{\boldsymbol{k},12}\Omega_{i,\boldsymbol{k}}\delta(\hbar\omega - E_{\boldsymbol{k},12})$$
$$= \frac{i\pi e^3}{\hbar^2 V}\sum_{\boldsymbol{k}} \Delta f_{\boldsymbol{k},12}\Delta v_{i,12}\Omega_{i,\boldsymbol{k}}\delta(\hbar\omega - E_{\boldsymbol{k},12}). \quad (4)$$

Here, $\Delta v_{i,12} = v_{i,1} - v_{i,2}$ is the velocity difference between the valence and conduction bands; $\Delta f_{\boldsymbol{k},12} = f_{\boldsymbol{k},1} - f_{\boldsymbol{k},2}$ is the Fermi distribution function between the valence and conduction bands. $\Omega_{i,\boldsymbol{k}} = i\epsilon_{ikl}\sum_{n\neq m} r^k_{\boldsymbol{k},nm} r^l_{\boldsymbol{k},mn}$ is the ith component of the Berry curvature. It is to be noted here that $\Delta f_{\boldsymbol{k},12}$, reducing to ± 1, plays a very crucial role in order to allow the participation of the WNs for a given value of chemical potential μ. This factor together with the δ function determine the frequency dependence of the CPG response. We consider $\omega > 0$ to investigate meaningful transport properties.

Based on the linearized, untilted, isotropic model $\boldsymbol{k}\cdot\boldsymbol{\sigma}$ for WNs, it has been shown that the CPG trace measures the Berry flux penetrating through a surface [31]. Therefore, the topological charge C of the WN, enclosed by the closed surface, results in a quantized CPG response. The quantization is observed in a certain frequency window, which can be generically dependent on chemical potential μ. Another interesting feature encoded in the δ function is that the CPG response shows a quantized response as long as ω is kept between two WN energies E_L and E_R, i.e., $2|E'_L| < \omega < 2|E'_R|$ with $E'_{L,R} = E_{L,R} - \mu$. For $\omega > 2|E'_R|$, the other Weyl node contributes with opposite sign in the Berry flux and the quantization is generically lost.

To complete the discussion, here we present the Berry curvature associated with the topological WSM Hamiltonian. The Berry curvature of the mth band for a Bloch Hamiltonian $H(k)$, defined as the Berry phase per unit area in the k space, is given by [54]

$$\Omega^m_a(\boldsymbol{k}) = (-1)^m \frac{1}{4|N_{\boldsymbol{k}}|^3}\epsilon_{abc} N_{\boldsymbol{k}}\cdot\left(\frac{\partial N_{\boldsymbol{k}}}{\partial k_b}\times\frac{\partial N_{\boldsymbol{k}}}{\partial k_c}\right). \quad (5)$$

B. Lattice Hamiltonian for IS and TRS broken WSM

We consider the following two-band Hamiltonian for the single WSM [31]: $\mathcal{H}^I(\boldsymbol{k}) = N_{\boldsymbol{k}}\cdot\boldsymbol{\sigma} + N_{0,\boldsymbol{k}}\sigma_0$, with

$$N_{\boldsymbol{k}} = \left(t_1\sin k_x, t_1\sin k_y, -M + t_1\sum_{i=x,y,z}\cos k_i\right)$$
$$= (N_{1,\boldsymbol{k}}, N_{2,\boldsymbol{k}}, N_{3,\boldsymbol{k}}),$$
$$N_{0,\boldsymbol{k}} = \gamma\sin k_z + t_2\cos k_z, \quad (6)$$

where σ^0 is the 2×2 identity matrix and $\boldsymbol{\sigma} = (\sigma^x, \sigma^y, \sigma^z)$ are the Pauli matrices. The Hamiltonian (6) breaks TRS and IS: $\mathcal{T}\mathcal{H}^I(-\boldsymbol{k})\mathcal{T}^{-1} \neq \mathcal{H}^I(\boldsymbol{k})$ with TR operator $\mathcal{T} = \mathcal{K}$, where $\mathcal{K}$ is a complex conjugation; $\mathcal{P}\mathcal{H}^I(-\boldsymbol{k})\mathcal{P}^{-1} \neq \mathcal{H}^I(\boldsymbol{k})$, with inversion operator $\mathcal{P} = \sigma_x$. We note that the Hamiltonian as represented in Eq. (6) preserves C_4 symmetry. The energy eigenvalues of $\mathcal{H}^I(\boldsymbol{k})$ are $E_{\boldsymbol{k},\pm} = N_{0,\boldsymbol{k}} \pm |N_{\boldsymbol{k}}|$, with

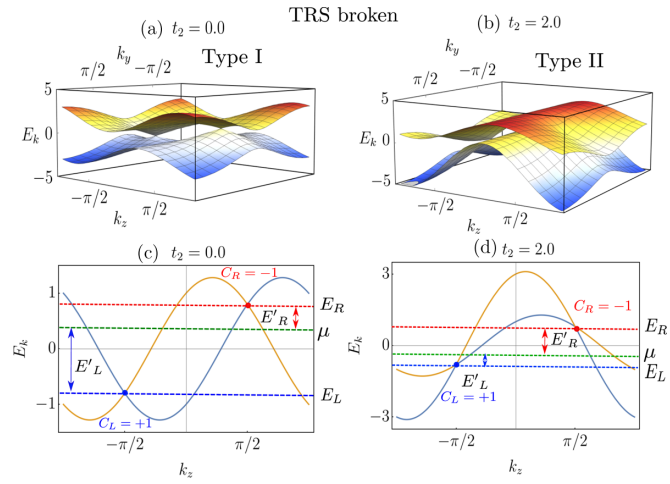

FIG. 1. The energy dispersion E_k for TRS broken WSMs is shown as a function of k_y and k_z for (a) type I and (b) type II. We repeat (a) and (b) considering $k_y = 0$ in (c) and (d). Two Weyl points at $k_z = \pm\pi/2$ are separated in energy $\epsilon_k = \pm\gamma$. The parameters considered here are $M = 2.0$, $\gamma = 0.8$, $t_1 = 1.0$, $t_2 = 0.0$ for type I, and $t_2 = 2.0$ for type II.

$|N_{\boldsymbol{k}}| = \sqrt{N^2_{1,\boldsymbol{k}} + N^2_{2,\boldsymbol{k}} + N^3_{1,\boldsymbol{k}}}$. For $1 < |M/t_1| < 3$, the model exhibits a pair of WNs of chirality s at $\boldsymbol{k}_{s=\mp} = (0, 0, \pm k_0)$, with energies $E_{\boldsymbol{k},s=\mp} = s\gamma\sin(k_0) + t_2\cos k_0$, where $k_0 = \cos^{-1}(M/t_1 - 2)$. The right-handed ($s = -1$) and left-handed ($s = +1$) WNs now appear, respectively, at $E_R = \gamma\sin k_0 + t_2\cos k_0$ and $E_L = -\gamma\sin k_0 + t_2\cos k_0$, producing a constant chiral chemical potential $\mu_{\mathrm{ch}} = (E_R - E_L)/2 = \gamma\sin k_0$, which is essential to obtain a nonzero CPG response. For $t_2/t_1 \to 0$ ($t_2/t_1 \to 1$), the model becomes a type-I (type-II) WSM. For $M = 2$ and $t_1 = 1$, the WNs appear at $\boldsymbol{k}_{\mp} = (0, 0, \pm\pi/2)$ associated with energies $E_{R,L} = \pm\gamma$ (see Fig. 1).

The low-energy Hamiltonian close to a WN with chirality s is given by

$$\mathcal{H}^I_{\boldsymbol{k},s} \approx s(\gamma - t_2 k_z)\sigma_0 + sk_x\sigma_x + sk_y\sigma_y + sk_z\sigma_z. \quad (7)$$

The Berry curvature takes the form $\Omega_i = \pm k_i/k^3$ $(i = x, y, z)$, with $k = \sqrt{k_x^2 + k_y^2 + k_z^2}$. Here, $\pm$ refers to the valence and conduction bands. The velocity takes the form $v_i = \pm sk_i/k$ $(i = x, y)$ and $v_z = \pm s(-t_2 + k_z/k)$. At the outset, we note that the term $\sum_i^{x,y,z}\Delta v_i\Omega_i$ in CPG trace (4) requires separate attention for the opposite chiral WNs: $\Delta v_i\Omega_i = k_i^2/k^4$ for left chiral WN ($s = +1$) and $\Delta v_i\Omega_i = -k_i^2/k^4$ for right chiral WN ($s = -1$). For $\mu \approx E_{L,R}$, we can consider the above low-energy model (7). Using the expressions (4) with $\Delta f = 1$, we then get the CPG response as follows:

$$\mathrm{Tr}[\beta(\omega)] \approx \frac{e^3\pi}{\hbar^2} i\int\frac{d\Omega}{(2\pi)^3}\int k^2 dk\sum_i^{x,y,z}\Delta v_i\Omega_i\frac{\delta(\omega/2 - E_{12})}{2}$$
$$\approx s\frac{e^3\pi}{\hbar^2} i\int\frac{d\Omega}{(2\pi)^3}\int k^2 dk\frac{\sum_i^{x,y,z} k_i^2}{k^4}\frac{\delta(\omega/2 - k)}{2}$$
$$= is\frac{e^3}{h^2}\oint_S d\boldsymbol{S}\cdot\boldsymbol{\Omega} = is\frac{e^3\pi}{h^2}C = is\beta_0. \quad (8)$$

Here, $d\Omega$ and $d\boldsymbol{S}$ are the element of the solid angle and surface area in a three-dimensional (3D) geometry associated with the spherical polar coordinate. The above formalism clearly shows that the CPG trace measures the Berry flux penetrating through $\boldsymbol{S}$ as discussed in Sec. II A. Therefore, the topological charge C of the WN, enclosed by the closed surface, results in a quantized CPG response. Hence, from the linearized model [Eq. (7)], as derived from the TRS broken Hamiltonian (6), one can find that the CPG response changes with the chirality of the WNs. This clearly suggests that $\mathrm{Tr}[\beta(\omega)]/i\beta_0$ acquires two opposite values when $\mu = E_R$ and $\mu = E_L$. The quantization window in terms of ω has already been discussed in Sec. II A. We would like to comment that the linearized model gives us a hint about the quantization; the lattice model, however, needs to be considered to get the detail of the CPG response.

We shall now address the issue of tilt in the above expression (8). We note that the effect of tilt can only enter in the CPG response through the Fermi distribution function Δf. Interestingly, Δv_i and Ω_i both are tilt independent as the tilt parameter t_2 appears in the σ_0 part of Eq. (7). The momentum integration for the tilted case would thus strongly depend on the apparently innocent factor Δf that becomes ± 1 for $T = 0$.

For completeness, here we discuss the explicit expressions of the Berry curvature $\boldsymbol{\Omega}(\boldsymbol{k}) = [\Omega_x(\boldsymbol{k}), \Omega_y(\boldsymbol{k}), \Omega_z(\boldsymbol{k})]$ and the velocity $\boldsymbol{v}(\boldsymbol{k}) = [v_x(\boldsymbol{k}), v_y(\boldsymbol{k}), v_z(\boldsymbol{k})]$ associated with Hamiltonian (6), given by

$$\begin{aligned}
\Omega_x &= \pm\frac{\cos k_y \sin k_x \sin k_z}{|N_{\boldsymbol{k}}|^3},\\
\Omega_y &= \pm\frac{\cos k_x \sin k_y \sin k_z}{|N_{\boldsymbol{k}}|^3},\\
\Omega_z &= \pm\frac{-\cos k_y + \cos k_x[-1 + \cos k_y(2 - \cos k_z)]}{|N_{\boldsymbol{k}}|^3},\\
v_x &= \pm\frac{(2 - \cos k_y - \cos k_z)\sin k_x}{|N_{\boldsymbol{k}}|},\\
v_y &= \pm\frac{(2 - \cos k_x - \cos k_z)\sin k_y}{|N_{\boldsymbol{k}}|},\\
v_z &= \gamma\cos k_z - t_2 \sin k_z\\
&\quad \pm \frac{(2 + \cos k_y + \cos k_z - \cos k_x)\sin k_z}{|N_{\boldsymbol{k}}|}. \qquad (9)
\end{aligned}$$

For a TRS broken WSM, here we find $\boldsymbol{\Omega}(\boldsymbol{k}) \neq -\boldsymbol{\Omega}(-\boldsymbol{k})$. Here, $\pm$ refers to the valence and conduction bands.

C. Lattice Hamiltonian for IS broken and TRS invariant WSM

The two-band model for the single WSM considered here is given by [55] $\mathcal{H}^{II}(\boldsymbol{k}) = N_{\boldsymbol{k}} \cdot \boldsymbol{\sigma} + N_{0,\boldsymbol{k}}\,\sigma_0$, with

$$\begin{aligned}
N_{\boldsymbol{k}} &= \{t_1[(\cos k_0 - \cos k_y) + \delta(1 - \cos k_z)],\\
&\quad t_1 \sin k_z, t_1[(\cos k_0 - \cos k_x) + \delta(1 - \cos k_z)]\}\\
&= (N_{1,\boldsymbol{k}}, N_{2,\boldsymbol{k}}, N_{3,\boldsymbol{k}}),\\
N_{0,\boldsymbol{k}} &= t_2[\cos(k_x + k_y) + \delta\cos(k_x - k_y)], \qquad (10)
\end{aligned}$$

where, t_1 and t_2 are the hopping parameters, and δ ($\neq 1$) is a constant. The Hamiltonian (10) breaks IS but preserves TRS: $\mathcal{T}\mathcal{H}^{II}(-\boldsymbol{k})\mathcal{T}^{-1} = \mathcal{H}^{II}(\boldsymbol{k})$ and $\mathcal{P}\mathcal{H}^{II}(-\boldsymbol{k})\mathcal{P}^{-1} \neq \mathcal{H}^{II}(\boldsymbol{k})$. It is noteworthy that the Hamiltonian as represented in Eq. (10) preserves $C_4\mathcal{T}$ symmetry. The energy eigenvalues of $\mathcal{H}^{II}_{\boldsymbol{k}}$ are $E_{\boldsymbol{k},\pm} = N_{0,\boldsymbol{k}} \pm |N_{\boldsymbol{k}}|$, with $|N_{\boldsymbol{k}}| = \sqrt{N^2_{1,\boldsymbol{k}} + N^2_{2,\boldsymbol{k}} + N^2_{3,\boldsymbol{k}}}$. For $t_2 = 0$ and $\delta > 1$, four gapless points arise in the $k_z = 0$ plane and, without any loss of generality, we can consider $0 < k_0 < \frac{\pi}{2}$. The right-handed ($s = +1$) WNs are located at $\boldsymbol{k}^{1,2}_{s=+} = \pm\,(k_0, k_0, 0)$ and the left-handed ($s = -1$) WNs are located at $\boldsymbol{k}^{1,2}_{s=-} \pm\ (k_0, -k_0, 0)$. When $t_2 \neq 0$, $N_{0,\boldsymbol{k}}$ causes a shift in the energies of the WNs of opposite chiralities. The right- and left-handed WNs now appear, respectively, at $E_R = t_2[\cos(2k_0) + \delta]$ and $E_L = t_2[1 + \delta\cos(2k_0)]$, producing a constant chiral chemical potential $\mu_{\mathrm{ch}} = (E_R - E_L)/2 = t_2(\delta - 1)\sin^2 k_0$, which is essential to obtain a nonzero CPG response. One can get type-I and type-II WSMs by tuning the ratio of $\frac{t_2}{t_1}$. For $\frac{t_2}{t_1} < 0.01$, two bands meet at four type-I WNs. For $\frac{t_2}{t_1} > 0.01$, the WNs start to tilt in the x direction and we have four type-II WNs. Considering $k_0 = \pi/4$, one finds two left chiral WNs at $\boldsymbol{k}^{1,2}_{-} = \pm(\pi/4, -\pi/4, 0)$ and two right chiral WNs at $\boldsymbol{k}^{1,2}_{+} = \pm(\pi/4, \pi/4, 0)$ with energies $E_L(E_R) = t_2(t_2\delta)$ [see Fig. 2].

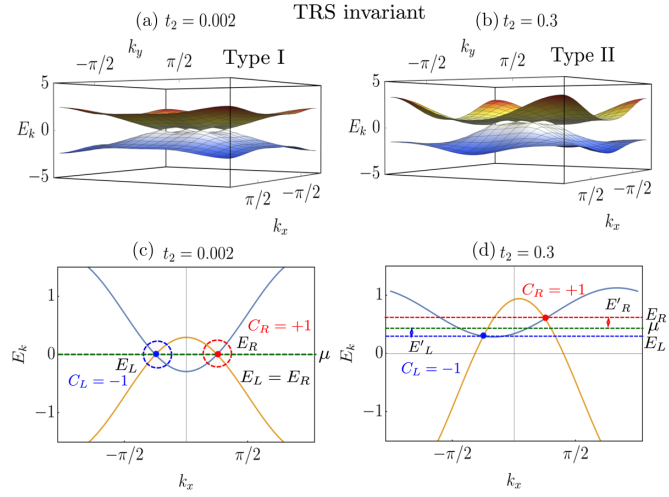

FIG. 2. The energy dispersion E_k for IS broken WSMs is shown as a function of k_y and k_z for (a) type I and (b) type II. We repeat (a) and (b) considering $k_y = 0$ in (c) and (d). Two Weyl points at $k_x = \pm\pi/4$ are separated in energy $E_R - E_L = t_2(\delta - 1)$. The parameters are $\delta = 2.0$, $t_1 = 1.0$, $t_2 = 0.002$ for type I, and $t_2 = 0.3$ for type II.

The low-energy Hamiltonian close to a given chiral node with chirality s is given by $\mathcal{H}^{II}{}_{\boldsymbol{k},s} \approx n_{s,0}\sigma_0 + t_1(sk_y + \delta k_z^2/2)\sigma_x + t_1 k_z\sigma_y + t_1(sk_x + \delta k_z^2/2)\sigma_z$, with $n_{s=-1,0} = t_2\delta(k_y - k_x) + t_2(1 - k_x k_y)$ and $n_{s=+1,0} = t_2\delta(1 + k_x k_y) - t_2(k_x + k_y)$. For simplicity, we consider $t_1 = 1$. One can now obtain the Berry curvature and the velocity difference around the right chiral WNs as $\Omega_i = \pm k_i/k^3$ and $\Delta v_i = k_i/k$. Following the same argument as presented for TRS broken WSM, we find the CPGE will be governed by the two right (left) chiral WNs when $\mu \approx E_R$ (E_L). To be precise, quantization would be twice the topological charge associated with the individual WNs as the contribution for two WNs with the same chirality gets added up. Therefore, the low-energy model suggests that the CPGE (8) for the TRS invariant case becomes twice that of the TRS broken case. Based on the

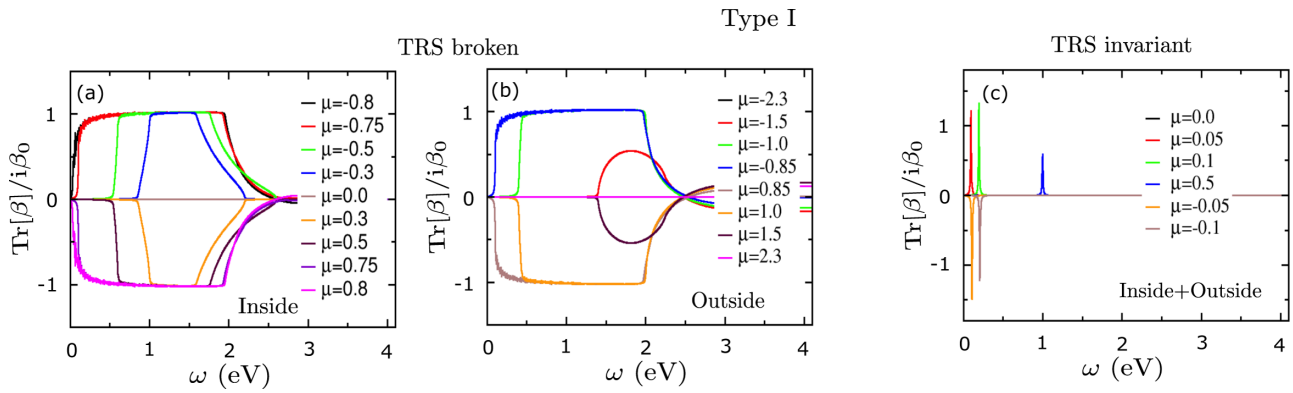

FIG. 3. (a),(b) Behavior of the CPG trace for a TRS broken type-I WSM. (c) IS broken type-I WSM for both the inside ($E_L < \mu < E_R$) and outside ($\mu < E_L$, $\mu > E_R$) regions. For the TRS broken case, the quantization in CPGE to two opposite values, which are given by the topological charge of the activated WN, is clearly observed when μ is set in between the two WN energies. Interestingly, when $E'_R = E'_L$, the CPG response appears to vanish; the CPGE shows nonquantized behavior when μ is well above and below the WN energies ($E_{R,L}$). In contrast, for the IS broken case, the CPGE is never found to be quantized in any of the above circumstances. We consider $\boldsymbol{k}$ mesh size $(500)^3$ for our numerical computations.

above argument considering the low-energy model, the CPGE is expected to show quantization at two exactly opposite values irrespective of the details of the lattice model. We shall investigate the validity of this expectation extensively in Sec. III by examining the lattice models (6) and (10).

For completeness, the explicit expressions of the Berry curvature $\boldsymbol{\Omega}(\boldsymbol{k}) = [\Omega_x(\boldsymbol{k}), \Omega_y(\boldsymbol{k}), \Omega_z(\boldsymbol{k})]$ and the velocity $\boldsymbol{v}(\boldsymbol{k}) = [v_x(\boldsymbol{k}), v_y(\boldsymbol{k}), v_z(\boldsymbol{k})]$ associated with the Hamiltonian (10) are given by

$$
\begin{aligned}
\Omega_x &= \pm\frac{[-\delta + (\cos k_0 + \delta - \cos k_x)\cos k_z]\sin k_y}{|N_{\boldsymbol{k}}|^3},\\
\Omega_y &= \pm\frac{[-\delta + (\cos k_0 + \delta - \cos k_y)\cos k_z]\sin k_x}{|N_{\boldsymbol{k}}|^3},\\
\Omega_z &= \pm\frac{\sin k_x \sin k_y \sin k_z}{|N_{\boldsymbol{k}}|^3},\\
v_x &= \pm\frac{[\cos k_0 - \cos k_x + \delta(1-\cos k_z)]\sin k_x}{|N_{\boldsymbol{k}}|}\\
&\quad - t_2\delta\sin(k_x - k_y) - t_2\sin(k_x + k_y),\\
v_y &= \pm\frac{[\cos k_0 - \cos k_y + \delta(1-\cos k_z)]\sin k_y}{|N_{\boldsymbol{k}}|}\\
&\quad + t_2\delta\sin(k_x - k_y) - t_2\sin(k_x + k_y),\\
v_z &= \pm\frac{(2\delta^2 + \cos k_z)\sin k_z}{|N_{\boldsymbol{k}}|}\\
&\quad \pm\frac{\delta(2\cos k_0 - 2\cos k_z - \cos k_x - \cos k_y)\sin k_z}{|N_{\boldsymbol{k}}|}. \qquad (11)
\end{aligned}
$$

For a TRS invariant WSM, here we find $\boldsymbol{\Omega}(\boldsymbol{k}) = -\boldsymbol{\Omega}(-\boldsymbol{k})$. Here, $\pm$ refers to the valence and conduction bands. The structure of the Berry curvature and velocity over the lattice Brillouin Zone (BZ) cannot be fully captured by the low-energy model. Therefore, below we shall study the lattice model to get a more reliable understanding that could relate to the experimental findings.

III. RESULT AND DISCUSSIONS

Having discussed the formalism to compute the CPG tensor, we now investigate it for IS broken WSMs. To begin with, we numerically estimate the CPG trace for the TRS broken type-I Weyl semimetal (6), as shown in Figs. 3(a) and 3(b). Here we consider the chemical potential for both the inside and outside regions of two nondegenerate WNs. The WNs with topological charge $C_{R,L} = \mp 1$ appear at $E_{R,L} = \pm 0.8$ for $k_0 = \pm\pi/2$. Both the WNs with energies E_L and E_R are equally spaced below and above for the chemical potential $\mu = 0$, i.e., $E'_R = E'_L$ with $|E_{R,L} - \mu| = E'_{R,L}$. We find that the CPG trace vanishes irrespective of the value of the frequency for $\mu = 0$. On the other hand, for $\mu = \pm 0.8$, our investigation shows that the quantization in the CPG trace at ∓ 1 starts from $\omega = 0$ and lasts until $\omega \approx 2.0$. However, the CPG trace decreases for $\omega > 2.0$ and vanishes around $\omega \approx 3.2$. One can thus infer that the CPG response is dependent on $|E'_R - E'_L|$. Precisely, the region of the quantization is found inside the following frequency window: $2|E'_L| < \omega < 2|E'_R|$.

We shall now discuss the CPG response when μ is away from the WN energies. For the chemical potential $\mu = -0.3$, inside between two WNs with $|E'_L| < |E'_R|$, the frequency window for the quantization at $+1$ is $1.0 < \omega < 1.5$ [see Fig. 3(a)]. For $\mu = 0.3$, the value of the quantization reverses within the same energy windows as $|E'_L| > |E'_R|$. The underlying reason is that the transport is maximally governed by the nature of the activated WN, i.e., the magnitude (sign) of quantization depends on the topological charge (chirality) of that WN. However, we find that the CPG trace becomes finite within the frequency window $2|E'_L| < \omega < 2|E'_R|$. The frequency above (below) which the CPG trace starts (ends) showing quantized behavior decreases toward zero when E'_R and E'_L are maximally deviated from each other. As a result, for $\mu = \pm 0.8$ (± 0.3), one can find largest (smallest) frequency window for quantization. When the chemical potential is outside the energy window between the two WNs, but close to any of the WNs within the linear band touching region, the CPGE is also found to be quantized [see Fig. 3(b)]. As expected, the quantized value depends on the topological charge

of the activated WN. But when $\mu \gg E_R, E_L$, i.e., far away from the nontrivial band crossing, the CPG trace becomes nonquantized, acquiring a smaller value <1. Importantly, we find antisymmetric behavior of the CPG response symmetrically placed around $\mu = (E_L + E_R)/2$.

In contrary, for the IS broken case of type I, as shown in Fig. 3(c), the CPG trace is never found to be quantized within an extended window of ω in any of the above circumstances. One can observe a sharp peak for certain values of the chemical potential, otherwise it remains zero throughout the whole frequency range. It can acquire values such as >1 (<−1), which is larger (smaller) than the topological charge of a single WN. We note that the total number of Weyl points present in the system is four. Therefore, the nonquantized CPG trace can be, in principle, larger (smaller) than 1 (−1). Based on our analysis in these two species of type-I models, the CPG trace is able to capture the symmetry mediated transport in a distinct way. For the TRS broken model, the quantized value is proportional to the charge of the WN, while for the TRS invariant model, the quantization is absolutely absent, however, the magnitude can be larger than the topological charge. One can infer that in order to obtain a quantized response of the CPG trace for type-I WSMs, the breaking of TRS plays a very crucial role. However, the most essential condition to obtain a quantized response is to have a substantial energy gap between WNs of different chiralities. For the TRS invariant model (10), the above criterion is violated $[(E_R - E_L) = t_2(\delta - 1) = 0.002$ eV], while for the TRS broken model (6), it is satisfied $[(E_R - E_L) = 2\gamma = 1.6$ eV]. In order to understand this phenomenon in more detail, below we investigate the type-II analog of these models.

We shall now try to anchor the above numerical findings with a plausible physical understanding. We first refer to the CPGE formula given in Eq. (4) where the expression inside the $\boldsymbol{k}$ sum can be decomposed into two parts, namely, $\Delta f_{\boldsymbol{k},12}\Delta v_{i,12}\Omega_{i,\boldsymbol{k}}$ that does not depend on ω and the remaining part $\delta(\hbar\omega - E_{\boldsymbol{k},12})$ that only depends on ω. The CPGE obtained in Fig. 3(c) clearly refers to the fact that the response is dominated by the δ function as it acquires a finite value only within a very short interval of ω. A close inspection of Fig. 3(c) suggests that the CPGE only becomes finite for $\omega \simeq 2\mu + O(t_2)$. The CPGE is expected to show a finite response $2|E_L'| < \omega < 2|E_R'|$ with $E_{L,R}' = E_{L,R} - \mu$ [31]. Now for the present TRS invariant type-I WSM, E_L and E_R both become vanishingly small with $t_2 \to 0$. The frequency interval thus shrinks to $2(\mu - \eta_1) < \omega < 2(\mu - \eta_2)$, with $\eta_1 = t_2\delta$ and $\eta_2 = t_2$ and $\eta_{1,2} \to 0$ as $t_2 \to 0$. Hence the part $\delta(\hbar\omega - E_{\boldsymbol{k},12})$ only feeds the part $\Delta f_{\boldsymbol{k},12}\Delta v_{i,12}\Omega_{i,\boldsymbol{k}}$ in the momentum integral for ω centered around $\omega \simeq 2\mu - (\eta_1 + \eta_2)$ while computing $\mathrm{Tr}[\beta(\omega)]$. For the type-I case with $t_2/t_1 < 0.01$ and $\mu > t_2$, the peak position of the CPGE depends on μ for a fixed value of t_2 and δ while these two parameters determine the shift in the peak location from $\omega = 2\mu$. These features are clearly noticed in Fig. 3(c).

On the other hand, since the energies E_L and E_R of two WNs are substantially close to each other, optically activated momentum surfaces, determined by the factor $\Delta f_{\boldsymbol{k},12}\delta(\hbar\omega - E_{\boldsymbol{k},12})$, might embed the nonlinear band crossings. This can cause an apparent deviation from the quantization if there is any such extended region on ω within which $\delta(\hbar\omega - E_{\boldsymbol{k},12})$

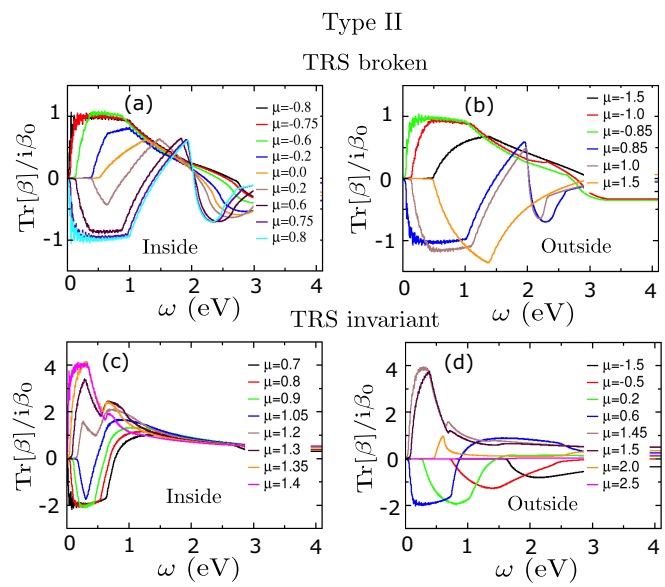

FIG. 4. (a),(b) Behavior of the CPG trace for the TRS broken type-II WSM. (c),(d) The IS broken type-II WSM for both inside ($E_L < \mu < E_R$) and outside ($\mu < E_L, \mu > E_R$) regions. For the TRS broken case, the quantization in the CPGE to two opposite values, which are given by the topological charge of the activated WN, is clearly observed when μ is set only around any of the Weyl point energy ($E_{R,L}$). Interestingly, when $E_R' = E_L'$, the CPGE does not vanish as with type I. For the IS broken case, the quantized value is noticed to be two times and four times the topological charge of the activated WNs when μ is set around E_L, E_R, respectively. We consider $\boldsymbol{k}$ mesh size $(500)^3$ for our numerical computations.

acquires a finite value. The magnitude of the peak decreases when μ is substantially away from E_L, E_R, which might refer to the fact that the contribution coming from the optically activated momentum surface reduces. We note here that the CPGE is found to be quantized in several WSMs and multifold fermionic systems with considerably separated WNs in energy space using first-principle studies [32,34,56]. The nonquantized behavior of the CPGE, found in Fig. 3(c), is not expected to persist when μ_{ch} becomes finite. We believe that our findings on the TRS invariant type-I WSM are not universal for any such pairs of WNs that are sufficiently separated in energy space. However, for TRS invariant WSM lattice models with WNs at different energies, the CPGE has not been studied so far due to lack of such lattice models in the literature [4,6]. The conventional expectation of a quantized CPGE is solely based on the finite nature of μ_{ch} that, in our case, no longer holds, resulting in such an unconventional δ-function-like response.

Figures 4(a) and 4(b) show the CPG trace for IS and TRS broken tilted type-II WSMs. Here the quantization is only obtained when the chemical potential is kept near to the energy of one of the WNs. For $\mu = \pm 0.8$ and ± 0.75, the CPG trace is quantized with values ∓ 1 within the frequency windows $0.2 < \omega < 1.2$. This quantization window for a type-II WSM is almost half compared to that of the type-I WSM with the same value of the chemical potential. The tilt modifies the available states near the Fermi surface (otherwise point like for the type-I untilted case) appearing in the CPG trace through the Fermi distribution function (Δf_{12}) associated with

the $\boldsymbol{k}$ modes in the BZ. The tilt thus imprints its effect by eventually normalizing the frequency window within which the CPG response acquires a quantized value. Interestingly, when $E_L' = E_R'$ for $\mu = 0$, the CPG trace does not vanish like type I, rather it shows nonquantized behavior.

When $E_L < \mu < E_R$ is well separated from the Weyl point energies $E_{R,L} = \pm 0.8$, the CPG trace becomes nonquantized. Similar to the type-I WSM, we find that the CPG trace is also quantized even when μ is kept outside the energy window between WNs but close to one of the WNs, as shown in Fig. 4(b). However, for $\mu \gg |E_{R,L}|$, one can obtain a nonquantized value of the CPG trace that is larger or smaller in magnitude than the absolute value of the topological charge of the activated WN. Moreover, the antisymmetric nature of the CPG response is not observed for type II. These features in the type-II TRS broken WSM are in stark contrast to the type-I counterpart of the same model. As discussed above, the Fermi surface states contribute to the transport, and so any change in the Fermi surface character would be clearly visible in the CPG response for type-I and type-II TRS broken WSMs.

Now we analyze the CPG response for IS broken type-II WSMs, where we find the quantized response for $E_L < \mu < E_R$ kept close to the WN energy $E_L = t_2 = 0.7$ and $E_R = t_2\delta = 1.4$ [see Fig. 4(c)]. This behavior remains unaltered when μ is close to E_L or E_R but outside the energy window set by these energies [Fig. 4(d)]. Comparing with type-II TRS broken WSMs, we find that the TRS invariant type-II WSM behaves in an identical way as far as the quantization is concerned. The frequency window for the quantized response of the CPGE in the TRS invariant case with $\mu \approx E_L$ is larger than that for $\mu \approx E_R$. In the case in which TRS is broken, these two quantization windows appear to be similar. Surprisingly, the CPGE becomes quantized to two different values -2 and 4 for μ close to E_L and E_R, respectively. This suggests that the antisymmetric nature of the CPG response is lost considering μ is symmetrically placed around $(E_L + E_R)/2$. This is in complete contrast to the TRS broken case, where the magnitude of the quantized value depends only on the charge of the activated Weyl point. One can find that there exist two left (right) chiral Weyl points at E_L (E_R) with topological charge $C_L = -1$ ($C_R = +1$). When μ is set close to E_L, the transport is governed by both of these two left chiral WNs and they contribute additively, resulting in the CPGE being proportional to $2C_L$. On the other hand, when μ is close to E_R where there exist two right chiral WNs with $C_R = +1$, the CPGE is found to be quantized at $4C_R$ instead of $2C_R$. This can be understood in the following way: activated WNs contribute differently, i.e., the product of the Berry curvature and velocity difference in the CPG trace at the left and right chiral WNs are not identical for the TRS invariant model; whereas for the TRS broken model, the product of the Berry curvature and velocity difference behave in an identical fashion around two opposite chiral WNs, which leads to the perfectly antisymmetric nature of the CPG trace. We can thus comment that the transport in a type-II TRS broken WSM is intrinsically different from the TRS invariant model type-II WSM.

We would now like to understand our results more deeply from the physical point of view. Using the CPG tensor (4), one can find for the TRS broken WSM that $\mathrm{Tr}[\beta] \simeq \sum_{\boldsymbol{k}} f_{\boldsymbol{k},12} \sum_i^{x,y,z} \Delta v_{i,12}(\boldsymbol{k}) \Omega_i(\boldsymbol{k}) \delta(\omega - E_{\boldsymbol{k},12})$ with $A(\boldsymbol{k}, \mu) = f_{\boldsymbol{k},12} \sum_i^{x,y,z} \Delta v_{i,12}(\boldsymbol{k}) \Omega_i(\boldsymbol{k})$. It is better to focus on the CPG response when μ is chosen close to the WN energies as the transport is maximally controlled by the nature of the WNs. For a TRS broken WSM, we can infer that $A(\boldsymbol{k}_s, \mu \approx E_{R,L}) \simeq s \sum_i^{x,y,z} \Delta v_{i,\boldsymbol{k}_s} \Omega_{i,\boldsymbol{k}_s}$ where $s = \mp 1$ substantially dominates in determining the behavior of $\mathrm{Tr}[\beta]$. A close inspection, considering the low-energy model, suggests that $A(\boldsymbol{k}_-, \mu \approx E_R) = -A(\boldsymbol{k}_+, \mu \approx E_L)$ as $\boldsymbol{\Omega}(\boldsymbol{k}_+) = \boldsymbol{\Omega}(\boldsymbol{k}_-)$ and $\Delta \boldsymbol{v}(\boldsymbol{k}_+) = -\Delta \boldsymbol{v}(\boldsymbol{k}_-)$. This leads to the fact that the injection current changes its sign as μ switches from left chiral WN energy to right chiral WN energy. In order to anchor this analytical analysis, we study $A(k_x = 0, k_y, k_z, \mu)$ numerically from the lattice model (6) in Figs. 5(a) and 5(b) for $\mu = -0.8$ and 0.8, respectively. We find that the sign of A reverses for $\mu = \pm 0.8$ with $k_y > 0$. The WN at $\boldsymbol{k}_+ = (0, 0, -\pi/2)$ for $\mu = -0.8$ actively participates in the CPGE quantization with positive magnitude in the sense that a kink is observed in A; the same observation, but negative in magnitude, is also noticed for the WN at $\boldsymbol{k}_- = (0, 0, \pi/2)$ with $\mu = 0.8$.

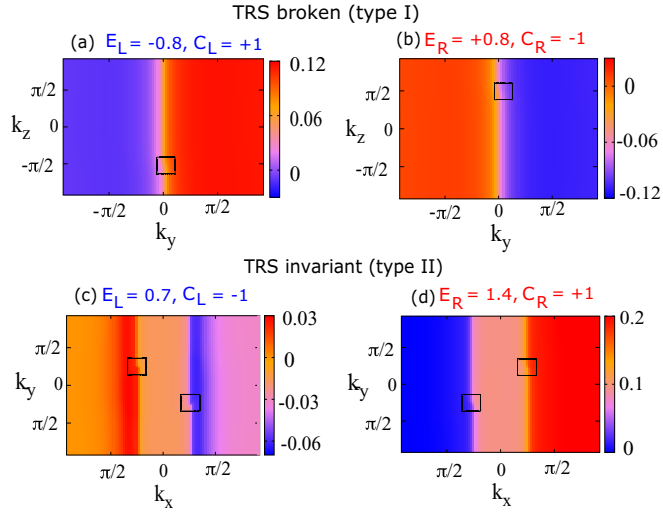

FIG. 5. The k-resolved plots $A(\boldsymbol{k}, \mu)$, (a),(b) for the TRS broken Hamiltonian $\mathcal{H}^I(\boldsymbol{k})$, and (c),(d) for the TRS invariant Hamiltonian $\mathcal{H}^{II}(\boldsymbol{k})$ with $\mu = E_L, E_R$, respectively. Here we consider $t_2 = 0$ and $\gamma = 0.8$ in $\mathcal{H}^I(\boldsymbol{k})$; $t_2 = 0.7$ and $\delta = 2.0$ in $\mathcal{H}^{II}(\boldsymbol{k})$. The position of the WNs is marked by a square. Comparing the momentum structure of A, one can infer that the CPGE at $\mu = E_L$ acquires opposite values to that at $\mu = E_R$ in (a) and (b) for TRS broken WSMs, whereas the CPGE acquires opposite but nonantisymmetric values at $\mu = E_L$ and $\mu = E_R$ in (c) and (d) for TRS invariant WSMs.

We will now analyze the TRS invariant case where four Weyl points are found: two left chiral WNs at $\boldsymbol{k}_-^{1,2} = \pm(\pi/4, -\pi/4, 0)$ with $E_L = t_2$ and two right chiral WNs at $\boldsymbol{k}_+^{1,2} = \pm(\pi/4, \pi/4, 0)$ with $E_R = t_2\delta$. When $\mu \approx E_L$, the left chiral nodes contribute maximally to the CPG tensor, $\mathrm{Tr}[\beta] \simeq \sum_{\boldsymbol{k}} \sum_i^{1,2} A(\boldsymbol{k}_-^i, \mu \approx E_L) \delta(\omega - E_{\boldsymbol{k},12})$. The analysis from the low-energy model refers to the fact that the CPGE acquires $2si\beta_0$ as the contribution from two WNs with same chirality gets added up. Therefore, the nonantisymmetric behavior of the CPGE trace as observed in Figs. 4(c) and 4(d) cannot be explained by the low-energy model. The structure of $\Omega(\boldsymbol{k}) = -\Omega(-\boldsymbol{k})$, as observed in TRS invariant WSMs, cannot be captured in the corresponding low-energy model. The same also

applies for the velocity difference Δv. These can result in a distinct behavior as compared to the low-energy model, while a TRS invariant lattice model is considered. Interestingly, in the TRS broken case, all three components of the CPG tensor i.e., β_{xx}, β_{yy}, and β_{zz}, contribute equally, i.e., $\beta_{xx} = \beta_{yy} = \beta_{zz}$, irrespective of the fact of whether $\mu \approx E_L$ or E_R. For the TRS invariant WSM, this analogy breaks, $\beta_{xx} = \beta_{yy} = \beta_{zz}/2 = i\beta$. More interestingly, the magnitude of the individual component $|i\beta|$, evaluated for $\mu \approx E_L$, gets doubled $2|i\beta|$ while computed for $\mu \approx E_R$. This causes the sharp contrast to the TRS broken case, where the magnitude of quantization for the CPG response becomes identical for both the chemical potentials $\mu \approx E_L$ and $\mu \approx E_R$. Furthermore, the frequency window for the quantized CPGE in this case becomes different for $\mu \approx E_R$ and E_L. By contrast, this frequency window for the TRS broken case is similar.

In order to anchor this analysis, we show $A(k_x, k_y, k_z = 0, \mu)$ numerically from the lattice model (10) in Figs. 5(c) and 5(d) for $\mu = E_L = 0.7$ and $\mu = E_R = 1.4$, respectively. We find that the sign of A reverses between $k_x > \pi/4$ and $k_x < -\pi/4$ with $\mu = 0.7$, while for $-\pi/4 < k_x < \pi/4$, $A(k_x, k_y, k_z = 0, \mu = E_L) \sim 0$. A exhibits a kink close to the Weyl point $\boldsymbol{k}_-^{1,2} = \pm(\pi/4, -\pi/4, 0)$ for $\mu = 0.7$, rendering the fact that these two left chiral nodes actively participate in the CPGE quantization which is found to be -2, while for $\mu = 1.4, A > 0 (\sim 0)$ for $k_x > -\pi/4$ $(< -\pi/4)$; however, the value of A increases for $k_x > \pi/4$ as compared to the value of A for $-\pi/4 < k_x < \pi/4$. Here, A exhibits kinks close to the right chiral Weyl point $\boldsymbol{k}_+^{1,2} = \pm(\pi/4, \pi/4, 0)$, suggesting the fact that these WNs actively participate in the quantization in the CPG response which has the value 4.

The momentum integration of A over the BZ for the TRS broken WSM becomes negative (positive) when $\mu = 0.8$ $(\mu = -0.8)$, as shown in Fig. 5(a) [Fig. 5(b)]. This is directly reflected in the behavior of the CPG tensor for $\mu = \pm 0.8$. Once μ reduces (increases) from 0.8 (-0.8), the magnitude of A decreases in the BZ for $k_y > 0$. For $\mu = 0$, A becomes vanishingly small in the BZ. As a result, the quantization is observed for $-0.8 \leqslant \mu \leqslant 0.8$, except $\mu = 0$. These above nature of the momentum distribution of A is also qualitatively valid for the tilted type-II case. However, unlike the type-I case, the tilt can destroy the quantization when μ is away from ± 0.8 within the window $-0.8 \leqslant \mu \leqslant 0.8$. The nonzero value of the CPG tensor for $\mu = 0$ in the type-II case is due to the anisotropic nature of the dispersion which is imprinted in A through the Fermi distribution function Δf_{12}.

The lattice analysis of A further reveals that it can have both positive and negative contributions in the BZ for the TRS invariant WSM with $\mu = 0.7$, as shown in Fig. 5(c). Upon increasing $\mu > 0.7$, one can find that A reduces for $k_x < -\pi/4$. A increases and becomes positive when μ reaches 1.4 when $k_x < -\pi/4$. In the intermediate zone $-\pi/4 < k_x < \pi/4$, A increases when μ increases from 0.4 to 1.4. For $\mu = 1.4$, A only acquires positive values for $k_x > \pi/4$, as shown in Fig. 5(d). From the momentum distribution of A for the TRS invariant WSM, it is evident that A does not show any antisymmetric behavior as observed for the TRS broken WSM when μ is kept at two different Weyl point energies E_L and E_R. This again points towards the fact that the CPG response can be very different for TRS broken and TRS invariant WSMs in terms of the quantization. On the other hand, for the type-I TRS invariant WSM, A turns out to be vanishingly small but antisymmetric with respect to the $k_x = 0$ plane in the BZ. As a result, the CPG response becomes characteristically different from the tilted case.

The exact quantization in the CPG trace is predicted from the $\boldsymbol{k} \cdot \boldsymbol{\sigma}$ model. The quantization can be destroyed due to several lattice effects. Away from the WNs, band bending causes the deviation of the CPG response from the quantized value. This quantization is clearly observed when μ is set close to the WN energy. On a general note, we can infer that for a type-II WSM, the band bending near the WNs affects the quantization more compared to type I. The band bending is more prominent in type II and that can result in the nonlinear correction to the quantization. In addition, we would like to note for experimental observability that the prefactor β_0 of Eq. (4) is large in comparison to ordinary CPG trace magnitudes. Considering typical relaxation times, one can find that the other metallic or insulating contributions are less than an order of magnitude as compared to the quantized WN contribution [51,57]. As a result, we believe the total CPG trace observed in experiment can signal the quantization [43].

We note that due to the lack of availability of the TRS invariant WSM lattice model hosting WNs of opposite chirality at two different energies, we could not generalize our findings in other TRS invariant WSM models with $\mu_{\rm ch} \neq 0$ [4,6,58]. Interestingly, $\mu_{\rm ch}$ changes with tilt parameter for our present model (10) that further causes the CPGE to behave distinctly in type-I and type-II phases (see Figs. 3 and 4). In general, due to the change in Fermi surface properties, type-II WSMs exhibit many intriguing transport signatures [27]. On the other hand, the low-energy model, generically defined for a single WN, might not distinguish a TRS invariant WSM from a TRS broken WSM. Our study suggests that the CPGE for a TRS invariant WSM cannot be thoroughly explained by the low-energy model contrasting the CPG response for a TRS broken WSM. This refers to the fact that the lattice model is indispensable in the present case of a TRS invariant WSM [59]. Unlike the TRS broken WSM hosting a single Fermi arc of definite chirality, the TRS invariant WSM supports a pair of chiral Fermi arcs. This has a severe implication for transport properties such as DC and optical conductivities [60,61]. We emphasize that our work thus uncovers various aspects of the transport signatures while investigating appropriate lattice models for tilted WSMs in the presence as well as absence of TRS. Therefore, our findings indeed convey a general picture that is not limited to the specific models considered here, as the conventional expectations are equally valid and are emerged from the same physical origins.

IV. CONCLUSION

We consider TRS invariant and TRS broken WSMs to study the CPG response where the energies E_L and E_R, associated with the left and right chiral Weyl points, are different from each other, $E_L \neq E_R$. The motivation is to analyze the

effect of TRS on the quantization, while the IS and mirror symmetries are already broken for both these WSMs. We consider a general tilted lattice Hamiltonian which allows us to additionally investigate the effect of tilted dispersion in the CPG response. There exist only two WNs of opposite chirality in a TRS broken system, while at least four WNs of opposite chiralities are present in a TRS invariant WSM. Therefore, when the number of WNs for a given chirality is more than unity, that could become an interesting situation to study. To be precise, a relevant question here is, how does the quantization depend on the number of WNs? In this work, we show that quantization for a TRS invariant single WSM can be two and four times the topological charge of the activated WNs (see Fig. 4). This feature is not observed for a TRS broken WSM as there exists only one WN for a given chirality (see Fig. 3). In addition, the CPG response is able to distinguish a type-II from a type-I WSM in general. It is noteworthy that a nonquantized peak in the CPGE at a certain frequency, depending on the values of the chemical potential, is originated due to fact that $E_L \simeq E_R$ for a TRS invariant type-I WSM. This is in stark contrast to all other quantized CPG responses, where E_L and E_R are substantially separated from each other.

In particular, the Berry curvature and the velocity difference play very a important role in determining the behavior of CPG trace. The tilt is not able to change the Berry curvature for the anisotropic case from the isotropic case; however, the velocity along the tilt direction can become very different from the isotropic case. The effect of tilt enters through the Fermi distribution function in the CPG trace as the velocity difference remains independent of the tilt parameter. As a result, the CPG response for type II is distinguishably different from type I. For example, in the TRS broken type-I case, the CPG traces behave exactly opposite to each other when μ is symmetrically chosen around $\mu = (E_L + E_R)/2$. This feature is not observed for the tilted type-II case. Moreover, the CPG response can acquire values larger than the magnitude of the topological charge in the presence of the tilting. Interestingly, in our present case, the type-II TRS invariant can only exhibit quantization in the CPG trace, unlike the type-I counterpart where $E_L \approx E_R$. The magnitude of quantization for μ close to E_L and E_R strongly depends on the Berry curvature and velocity around the left and right chiral WNs. In the TRS broken WSM, the value of quantization for $\mu \sim E_L$ is just opposite to that for $\mu \sim E_R$. For the TRS invariant case, these two values of quantization are different from each other, as the Berry curvature and velocity (as well as the velocity difference) behave differently for left and right chiral WNs. We can comment that the low-energy model might not always predict the numerical findings, based on the lattice model, especially when there exists more that a single WN with a given chirality [58]. This is the case that we encounter in the TRS invariant WSM lattice Hamiltonian and the nonantisymmetric quantization of the CPGE there might not be explained by the associated low-energy model.

We believe that our observation can be tested experimentally due to the availability of the setup. It would be interesting to study the TRS broken and invariant chiral multi-WSM having nonlinear anisotropic dispersion. The band bending causes the CPGE to deviate from the quantized behavior. The role of TRS and band bending are two important aspects that can be studied in the future in chiral SMs [41–43].

ACKNOWLEDGMENTS

T.N. would like to thank MPIPKS, Dresden, Germany, for providing the computation facility. We would like to thank Adolfo G. Grushin for carefully reading the manuscript and giving his valuable comments.

[1] B. Yan and C. Felser, Annu. Rev. Condens. Matter Phys. **8**, 337 (2017).
[2] H. Weng, Nat. Mater. **18**, 428 (2019).
[3] P. Hosur and X. Qi, C. R. Phys. **14**, 857 (2013).
[4] N. P. Armitage, E. J. Mele, and A. Vishwanath, Rev. Mod. Phys. **90**, 015001 (2018).
[5] G. S. Jenkins, C. Lane, B. Barbiellini, A. B. Sushkov, R. L. Carey, F. Liu, J. W. Krizan, S. K. Kushwaha, Q. Gibson, T.-R. Chang, H.-T. Jeng, H. Lin, R. J. Cava, A. Bansil, and H. D. Drew, Phys. Rev. B **94**, 085121 (2016).
[6] T. M. McCormick, I. Kimchi, and N. Trivedi, Phys. Rev. B **95**, 075133 (2017).
[7] Y. Xu, F. Zhang, and C. Zhang, Phys. Rev. Lett. **115**, 265304 (2015).
[8] B. Lv, N. Xu, H. Weng, J. Ma, P. Richard, X. Huang, L. Zhao, G. Chen, C. Matt, F. Bisti *et al.*, Nat. Phys. **11**, 724 (2015).
[9] S.-Y. Xu, I. Belopolski, N. Alidoust, M. Neupane, G. Bian, C. Zhang, R. Sankar, G. Chang, Z. Yuan, C.-C. Lee *et al.*, Science **349**, 613 (2015).
[10] J. Jiang, Z. Liu, Y. Sun, H. Yang, C. Rajamathi, Y. Qi, L. Yang, C. Chen, H. Peng, C. Hwang *et al.*, Nat. Commun. **8**, 13973 (2017).
[11] P. Li, Y. Wen, X. He, Q. Zhang, C. Xia, Z.-M. Yu, S. A. Yang, Z. Zhu, H. N. Alshareef, and X.-X. Zhang, Nat. Commun. **8**, 2150 (2017).
[12] S.-i. Kimura, Y. Nakajima, Z. Mita, R. Jha, R. Higashinaka, T. D. Matsuda, and Y. Aoki, Phys. Rev. B **99**, 195203 (2019).
[13] K.-Y. Yang, Y.-M. Lu, and Y. Ran, Phys. Rev. B **84**, 075129 (2011).
[14] A. A. Burkov and L. Balents, Phys. Rev. Lett. **107**, 127205 (2011).
[15] D. T. Son and B. Z. Spivak, Phys. Rev. B **88**, 104412 (2013).
[16] S. Murakami, New J. Phys. **9**, 356 (2007).
[17] B. Sadhukhan, Y. Zhang, R. Ray, and J. van den Brink, Phys. Rev. Mater. **4**, 064602 (2020).
[18] A. A. Zyuzin and A. A. Burkov, Phys. Rev. B **86**, 115133 (2012).
[19] R. Ray, B. Sadhukhan, M. Richter, J. I. Facio, and J. v. d. Brink, arXiv:2006.10602.
[20] K. Landsteiner, Phys. Rev. B **89**, 075124 (2014).
[21] G. Sharma, P. Goswami, and S. Tewari, Phys. Rev. B **93**, 035116 (2016).
[22] T. Nag and S. Nandy, J. Phys.: Condens. Matter **33**, 075504 (2020).

[23] Y. Zhang, Q. Xu, K. Koepernik, C. Fu, J. Gooth, J. van den Brink, C. Felser, and Y. Sun, New J. Phys. **22**, 093003 (2020).
[24] M. Hirschberger, S. Kushwaha, Z. Wang, Q. Gibson, S. Liang, C. A. Belvin, B. A. Bernevig, R. J. Cava, and N. P. Ong, Nat. Mater. **15**, 1161 (2016).
[25] S. J. Watzman, T. M. McCormick, C. Shekhar, S.-C. Wu, Y. Sun, A. Prakash, C. Felser, N. Trivedi, and J. P. Heremans, Phys. Rev. B **97**, 161404(R) (2018).
[26] F. Fei, X. Bo, R. Wang, B. Wu, J. Jiang, D. Fu, M. Gao, H. Zheng, Y. Chen, X. Wang *et al.*, Phys. Rev. B **96**, 041201(R) (2017).
[27] Z.-M. Yu, Y. Yao, and S. A. Yang, Phys. Rev. Lett. **117**, 077202 (2016).
[28] S. Nandy, G. Sharma, A. Taraphder, and S. Tewari, Phys. Rev. Lett. **119**, 176804 (2017).
[29] T. Nag, A. Menon, and B. Basu, Phys. Rev. B **102**, 014307 (2020).
[30] C. Schindler, S. Galeski, W. Schnelle, R. Wawrzyńczak, W. Abdel-Haq, S. N. Guin, J. Kroder, N. Kumar, C. Fu, H. Borrmann *et al.*, Phys. Rev. B **101**, 125119 (2020).
[31] F. de Juan, A. G. Grushin, T. Morimoto, and J. E. Moore, Nat. Commun. **8**, 15995 (2017).
[32] F. Flicker, F. de Juan, B. Bradlyn, T. Morimoto, M. G. Vergniory, and A. G. Grushin, Phys. Rev. B **98**, 155145 (2018).
[33] C.-K. Chan, N. H. Lindner, G. Refael, and P. A. Lee, Phys. Rev. B **95**, 041104(R) (2017).
[34] Y. Zhang, H. Ishizuka, J. van den Brink, C. Felser, B. Yan, and N. Nagaosa, Phys. Rev. B **97**, 241118(R) (2018).
[35] D. E. Parker, T. Morimoto, J. Orenstein, and J. E. Moore, Phys. Rev. B **99**, 045121 (2019).
[36] Q. Xu, Y. Zhang, K. Koepernik, W. Shi, J. van den Brink, C. Felser, and Y. Sun, npj Comput. Mater. **6**, 32 (2020).
[37] Y. Zhang, F. de Juan, A. G. Grushin, C. Felser, and Y. Sun, Phys. Rev. B **100**, 245206 (2019).
[38] E. J. König, H.-Y. Xie, D. A. Pesin, and A. Levchenko, Phys. Rev. B **96**, 075123 (2017).
[39] T. Holder, D. Kaplan, and B. Yan, Phys. Rev. Research **2**, 033100 (2020).
[40] F. de Juan, Y. Zhang, T. Morimoto, Y. Sun, J. E. Moore, and A. G. Grushin, Phys. Rev. Research **2**, 012017(R) (2020).
[41] N. B. Schröter, D. Pei, M. G. Vergniory, Y. Sun, K. Manna, F. De Juan, J. A. Krieger, V. Süss, M. Schmidt, P. Dudin *et al.*, Nat. Phys. **15**, 759 (2019).
[42] S. Changdar, S. Aswartham, A. Bose, Y. Kushnirenko, G. Shipunov, N. C. Plumb, M. Shi, A. Narayan, B. Büchner, and S. Thirupathaiah, Phys. Rev. B **101**, 235105 (2020).
[43] Z. Ni, K. Wang, Y. Zhang, O. Pozo, B. Xu, X. Han, K. Manna, J. Paglione, C. Felser, A. G. Grushin *et al.*, Nat. Commun. **12**, 154 (2021).
[44] G. Xu, H. Weng, Z. Wang, X. Dai, and Z. Fang, Phys. Rev. Lett. **107**, 186806 (2011).
[45] C. Fang, M. J. Gilbert, X. Dai, and B. A. Bernevig, Phys. Rev. Lett. **108**, 266802 (2012).
[46] S.-M. Huang, S.-Y. Xu, I. Belopolski, C.-C. Lee, G. Chang, T.-R. Chang, B. Wang, N. Alidoust, G. Bian, M. Neupane, D. Sanchez, H. Zheng, H.-T. Jeng, A. Bansil, T. Neupert, H. Lin, and M. Z. Hasan, Proc. Natl. Acad. Sci. **113**, 1180 (2016).
[47] B. Singh, G. Chang, T.-R. Chang, S.-M. Huang, C. Su, M.-C. Lin, H. Lin, and A. Bansil, Sci. Rep. **8**, 10540 (2018).
[48] Q. Liu and A. Zunger, Phys. Rev. X **7**, 021019 (2017).
[49] S. Zhong, J. E. Moore, and I. Souza, Phys. Rev. Lett. **116**, 077201 (2016).
[50] M. Yao, K. Manna, Q. Yang, A. Fedorov, V. Voroshnin, B. V. Schwarze, J. Hornung, S. Chattopadhyay, Z. Sun, S. N. Guin *et al.*, Nat. Commun. **11**, 2033 (2020).
[51] I. Sodemann and L. Fu, Phys. Rev. Lett. **115**, 216806 (2015).
[52] H. Rostami and V. Juričić, Phys. Rev. Research **2**, 013069 (2020).
[53] J. E. Sipe and A. I. Shkrebtii, Phys. Rev. B **61**, 5337 (2000).
[54] X.-L. Qi, Y.-S. Wu, and S.-C. Zhang, Phys. Rev. B **74**, 085308 (2006).
[55] U. Dey, S. Nandy, and A. Taraphder, Sci. Rep. **10**, 2699 (2020).
[56] C. Le, Y. Zhang, C. Felser, and Y. Sun, Phys. Rev. B **102**, 121111(R) (2020).
[57] J. E. Moore and J. Orenstein, Phys. Rev. Lett. **105**, 026805 (2010).
[58] B. Sadhukhan and T. Nag, arXiv:2104.01629.
[59] V. Dwivedi and S. T. Ramamurthy, Phys. Rev. B **94**, 245143 (2016).
[60] I. Jang and K.-S. Kim, Phys. Rev. B **97**, 165201 (2018).
[61] C. J. Tabert, J. P. Carbotte, and E. J. Nicol, Phys. Rev. B **93**, 085426 (2016).